Numerical Simulations and Planar Laser-Induced Fluorescence Imaging Results of Hypersonic Reactive Flows

Kazu Toshimitsu*
Kyushu University, Fukuoka 812-81, Japan
Akiko Matsuo[†]
Keio University, Yokohama 223, Japan
and
Michel R. Kamel,[‡] Christopher I. Morris,[‡] and Ronald K. Hanson[§]
Stanford University, Stanford, California 94305-3032

This paper shows comparisons between computational fluid dynamics (CFD) calculations and planar laser-induced fluorescence and schlieren measurements of inert and reactive hypersonic flows around two-dimensional and axisymmetric bodies. In particular, both hydrogen–oxygen and methane–oxygen chemical reactions are considered for the shock-induced combustion in hypersonic flows. The hydrogen–oxidation mechanism consists of an existing mechanism of 8 reacting species and 19 elementary reactions. The reduced model of the methane-oxidation mechanism is newly derived from the GRI-Mech 1.2 optimized detailed chemical reaction mechanism, and consists of 14 species and 19 chemical reaction steps. Both chemical reaction mechanisms are combined with a point-implicit Euler CFD code. The OH species density distributions of the present numerical calculations and imaging experiments for both mixtures are found to be in qualitative agreement.

I. Introduction

IT is very important for the optimal design of ram accelerators that the flow characteristics around hypervelocity projectiles be well predicted by computational calculations. The characteristics of hydrogen–oxidation and methane–oxidation reactive flows around supersonic and hypersonic projectiles have been previously investigated.[1−11] These works have made clear the important role of the combustion mechanism, unsteadiness, viscous effects, and chemical kinetics in modeling reactive flows. However, a comparison of computational fluid dynamics (CFD) results with experimental data for species distribution profiles has not been carried out.

The Stanford expansion tube facility was used to obtain spatially and temporally resolved optical measurements of hypersonic reactive flowfields around several projectiles. Qualitative[12,13] and quantitative[14] planar laser-induced fluorescence (PLIF) imaging experiments of hypersonic inert and reactive flows over projectiles have been performed for comparison with the CFD calculations.

In this paper, the flowfields around a two-dimensional rod and axisymmetric hemisphere projectiles are investigated using a CFD program based on Matsuo's code.[10,11] A hydrogen–oxidation mechanism of 8 species and 19 chemical reaction steps is used for the hydrogen–oxygen–nitrogen mixtures. Furthermore, a reduced chemical reaction mechanism of 14 species and 19 chemical reaction steps is proposed for the CFD simulations of methane–oxygen–nitrogen mixtures. Through the comparison of CFD calculations and PLIF imaging results, the code accuracy, chemical kinetics, and the flowfield characteristics are investigated.

II. Numerical Formulation

The computational simulations are conducted on the following Euler equation for two-dimensional and axisymmetric flows with the species conservation equations:

$$\frac{\partial \hat{Q}}{\partial \tau} + \frac{\partial \hat{E}}{\partial \xi} + \frac{\partial \hat{F}}{\partial \eta} = \hat{S} + \hat{H} \tag{1}$$

where $\hat{E}$ and $\hat{F}$ are inviscid flux vectors in ξ and η coordinates, respectively. The term $\hat{S}$ means the chemical reaction source vector, and $\hat{H}$ is the axisymmetric source term. For a two-dimensional projectile, $\hat{H}$ is equal to 0. The numerical analyses are based on Yee's[15] non-MUSCL-type total variation diminishing (TVD) upwind explicit scheme for the conservation equation and an implicit integration of the chemical reaction processes, i.e., the so-called point-implicit scheme.

III. Numerical Results and Reaction Models

In the following three sections, the numerical results are presented according to the type of gas used in the calculations: air, hydrogen–oxygen–nitrogen, and methane–oxygen–nitrogen mixtures. The numerical and experimental conditions investigated in this work are listed in Table 1. To remove the dependence of mesh size on the numerical simulations, various mesh sizes are used in similar simulations and their results are compared. Convergence was satisfied when the value of the numerical residual decreased below $10^{-4.5}$ at the end of an iteration step. The convergence condition is given by

$$\sum_{i,j}^{N} \frac{\left| \rho_{i,j}^{t} - \rho_{i,j}^{t+\Delta t} \right|}{(N \rho_{\infty})} < 10^{-4.5} \tag{2}$$

where i and j are node numbers, N is total node number of the meshes, t is the time level, and ρ_{∞} is the density of incoming flow.

Both the accuracy and reliability of the code have already been established at least for density profiles of a hydrogen–oxygen mixture in another paper.[10] However, a comparison between PLIF imaging results and CFD calculations for OH species profile has not been performed. Hence, we will mainly discuss the comparison of them in the following sections. For the inert gas experiments, NO PLIF and schlieren imaging measurements have been applied to obtain the

Table 1 Investigated conditions

Number	U_∞, m/s (M)	p_∞, kPa (psi)	T_∞, K	Mixture, mole %	Mesh size	Projectile	Experiment
				O_2/N_2			
1	2230 (7.0)	6.4 (0.94)	280	21.0/79.0 (inert)	76 × 51 151 × 151	Hemisphere (d = 19 mm)	NO PLIF
				$H_2/O_2/N_2$			
2	1960 (5.2)	11.2 (1.65)	350	10.0/5.0/85.0	101 × 101 151 × 151	Hemisphere (d = 19 mm)	OH PLIF
				$CH_4/O_2/N_2$			
3	2330 (6.8)	50 (7.11)	295	9.5/19.0/71.5	76 × 51 101 × 81 151 × 101	Rod (d = 1, 3, and 7 mm)	——
4	2150 (6.8)	20 (2.94)	260	16.7/33.3/50.0	151 × 151	Hemisphere (d = 19 mm)	——
5	(6.8)	10 (1.47)	260	16.7/33.3/50.0	151 × 151	Hemisphere (d = 19 mm)	——
6	(6.8)	6.4 (0.91)	260	16.7/33.3/50.0	151 × 151	Hemisphere (d = 19 mm)	OH PLIF

Note: U_∞, p_∞, and T_∞ denote velocity at freestream, static pressure, and static temperature, respectively.
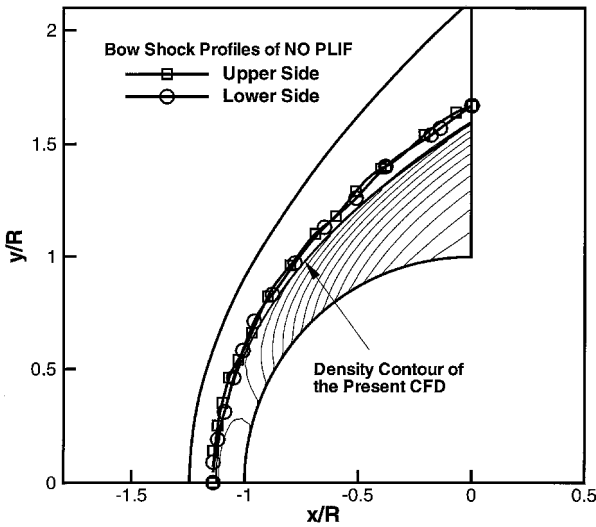
Fig. 1 Comparison of bow-shock profiles by CFD calculation and NO PLIF measurement around the hemispheric body in condition 1.

shock profiles for hypersonic flows around a hemispherical cylinder. OH PLIF and schlieren imaging measurements were used for the reactive cases, with the OH PLIF showing the regions of combustion and schlieren imaging used to visualize the shock wave.

A. Inert Gas (Air)

For the hemispherical body of condition 1, a 151 × 151 mesh size was used to calculate the density contour and to show the bow-shock shape and position. The result was compared to NO PLIF measurements as shown in Fig. 1. The agreement between the calculated shock position and the imaged one is good on the centerline ($y/R = 0$). The described example indicates that the CFD calculations are useful for predicting the inert gas flowfields around the axisymmetric hemisphere projectiles.

B. H_2–O_2 Shock-Induced Combustion

The hydrogen-oxidation mechanism used in this work consists of 8 species (H_2, O_2, H, O, OH, H_2O, HO_2, and H_2O_2) and 19 chemical reaction steps, which are shown in Table 2 (Ref. 10). It is reduced from the mechanisms of Jachimowski[16] and Wilson and MacComack[1] because the nitrogen reactions are not important at Mach numbers less than 5.

Table 2 H_2–O_2 Reaction Mechanism[10]

k	Reaction	A	n	E
1	$H_2 + O_2 = HO_2 + H$	1.00×10^{14}	0.0	56,000
2	$H + O_2 = OH + O$	2.60×10^{14}	0.0	16,800
3	$O + H_2 = OH + H$	1.80×10^{10}	1.0	8,900
4	$OH + H_2 = H + H_2O$	2.20×10^{13}	0.0	5,150
5	$2OH = O + H_2O$	6.30×10^{12}	−2.0	1,090
6	$H + OH + M = H_2O + M$	2.20×10^{22}	−1.0	0
7	$2H + M = H_2 + M$	6.40×10^{17}	−0.6	0
8	$H + O + M = OH + M$	6.00×10^{16}	0.0	0
9	$H + O_2 + M = HO_2 + M$	2.10×10^{15}	0.0	−1,000
10	$2O + M = O_2 + M$	6.00×10^{13}	0.0	−1,800
11	$HO_2 + H = 2OH$	1.40×10^{14}	0.0	1,080
12	$HO_2 + H = H_2O + O$	1.00×10^{13}	0.0	1,080
13	$HO_2 + O = O_2 + OH$	1.50×10^{13}	0.0	950
14	$HO_2 + OH = H_2O + O_2$	8.00×10^{12}	0.0	0
15	$2HO_2 = H_2O_2 + O_2$	2.00×10^{12}	0.0	0
16	$H + H_2O_2 = H_2 + HO_2$	1.40×10^{12}	0.0	3,600
17	$O + H_2O_2 = OH + HO_2$	1.40×10^{13}	0.0	6,400
18	$OH + H_2O_2 = H_2O + HO_2$	6.10×10^{12}	0.0	1,430
19	$H_2O_2 + M = 2OH + M$	1.20×10^{17}	0.0	45,500

Note: $k_f = AT^n \exp(-E_k/RT)$; units are in second, moles, centimeters, calories, and Kelvins.
Third body efficiencies relative to N_2: reaction 6 $H_2O = 6.0$, reaction 7 $H_2O = 6.0$ and $H_2 = 2.0$, reaction 8 $H_2O = 5.0$, reaction 9 $H_2O = 16.0$ and $H_2 = 2.0$, and reaction 19 $H_2O = 15.0$.

Figure 2 shows the OH species density distributions and bow-shock profiles calculated using the CFD (mesh size 151 × 151) and OH PLIF and schlieren measurements[13] around a hemispheric body in condition 2. Both the bow-shock and OH species profiles are in good agreement. This demonstrates that the CFD code can correctly simulate the hypersonic-re-active flowfield experiments (shock-induced combustion of a hydrogen–oxygen–nitrogen mixture) generated in the Stanford expansion tube facility.

C. CH_4–O_2 Shock-Induced Combustion

1. Reaction Mechanism

Many detailed and reduced mechanisms of methane–oxidation chemical reaction have been suggested. For example, the 19-species 52-reaction mechanism proposed by Yungster and Rabinowitz[6] has a good accuracy; however, it is still complex and requires large computational power, e.g., a Cray parallel supercomputer, to calculate the hypersonic reactive flowfield. In this section, a new reduced chemical kinetic model is proposed to calculate (using a standard computer, e.g., a Hewlett Packard HP9000/712) the characteristics of methane–oxidation reactive

CFD GRAPHIC DATA

Density Contour

[OH]

8.00E-3
7.20E-3
6.40E-3
5.60E-3
4.80E-3
4.00E-3
3.20E-3
2.40E-3
1.60E-3
8.00E-4
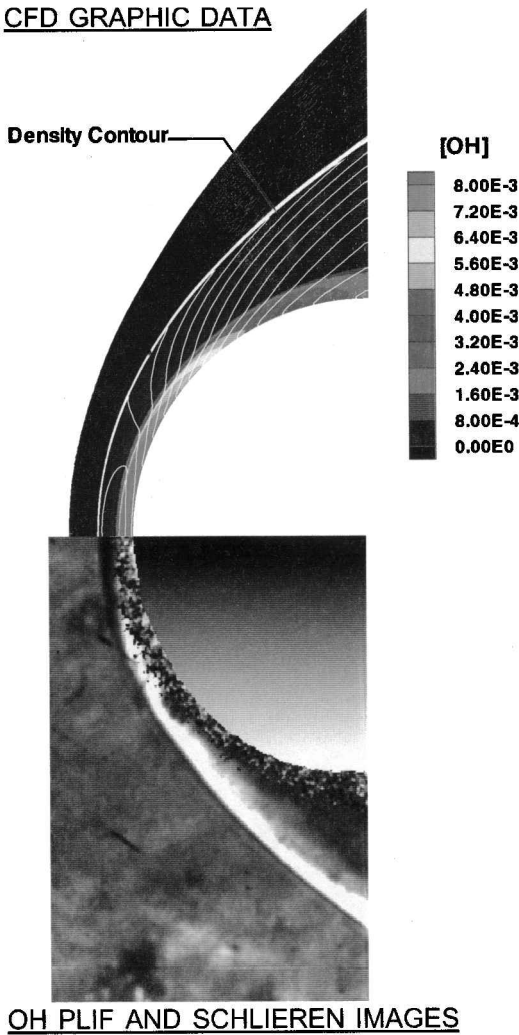0.00E0

OH PLIF AND SCHLIEREN IMAGES

Fig. 2   Comparison of OH species density distributions and bow-shock profiles by CFD calculation, OH PLIF, and schlieren imaging results around the hemispheric body in condition 2.

flows under 3.0 MPa pressure. The chemical reaction model is reduced from the full mechanism of GRI-Mech 1.2 (Ref. 17) through the sensitivity analyses of GRI-Mech 1.2 (Ref. 18) and the Senkin program.[19] The mechanism consists of 14 species (H_2, O_2, H, O, OH, H_2O, CH_3, CH_4, CO, CO_2, HCO, CH_2O, CH_3O, and C_2H_6) and 19 chemical reaction steps. Its rate coefficients are listed in Table 3. To compare the accuracy of the different chemical kinetic models, temperature and OH mole fraction profiles are calculated using Chemkin[20] at two different conditions: 1) 2600 K and 3.0 MPa and 2) 2200 K and 0.4 MPa, under constant internal energy and volume. The three different chemical kinetic models used in this comparative study are the GRI-Mech 1.2 mechanism, the Yungster and Rabinowitz mechanism[6] and the present 14-species and 19-chemical reactions model with pressure dependence rate coefficients of the Troe formulas.[21] Those are derived from the data at the stagnation point of the O_2-N_2 nonreactive mixtures in conditions 3 and 6 (Table 1) by the present CFD analyses. Figures 3 and 4 show temperature and OH mole fraction in conditions 1 and 2, respectively. Those of the GRI-Mech 1.2 mechanism, the Yungster and Rabinowitz mechanism,[6] and the present 19 steps are in good agreement in condition 1. In condition 2, the ignition times of the present 19-step model exhibit delays of 2 μs from the ones of both the GRI-Mech 1.2 and Yungster and Rabinowitz mechanisms. However, in condition 2, i.e., in condition 6, the delay time may cause ~1 mm error of reaction front standoff distance. That means the delay effect on the reaction front position is small. Effects on the CFD simulations are discussed in Secs. III.C.2 and III.C.3.
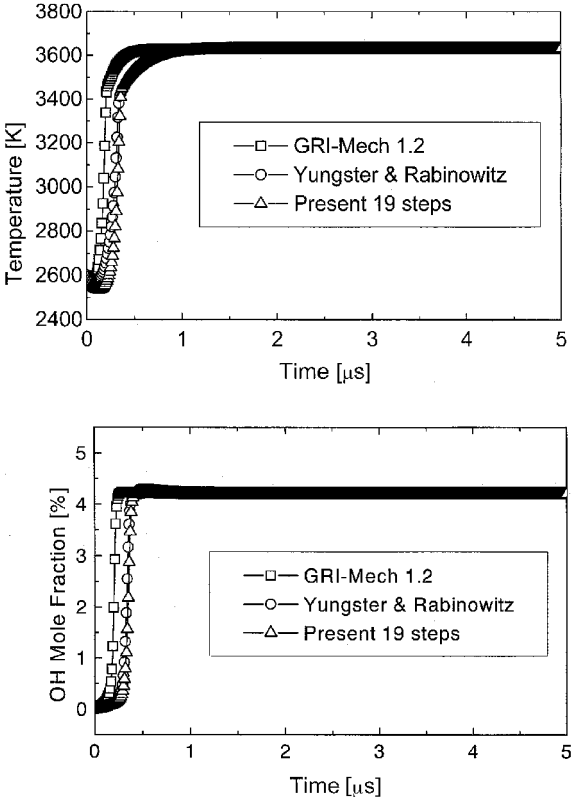
Fig. 3   Temperatures and OH mole fractions of GRI-Mech 1.2, Yungster and Rabinowitz,[6] and present chemical models at 2600 K and 3.0 MPa.
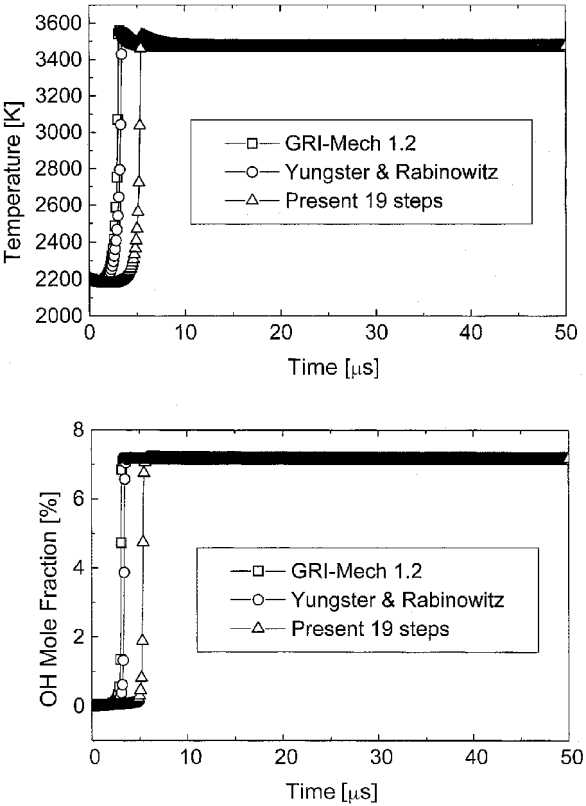
Fig. 4   Temperatures and OH mole fractions of GRI-Mech 1.2, Yungster and Rabinowitz,[6] and present chemical models at 2200 K and 0.4 MPa.

Table 3   CH$_4$–O$_2$ Reaction Mechanism

k	Reaction	A	n	E
1	H + O$_2$ = O + OH	8.300×10^{13}	0.000	14,413
2	O + H$_2$ = H + OH	5.000×10^{4}	2.670	6,290
3	OH + H$_2$ = H + H$_2$O	2.160×10^{8}	1.510	3,430
4	H + OH + M = H$_2$O + M	2.200×10^{22}	−2.000	0
5	OH + CO = H + CO$_2$	4.760×10^{7}	1.228	70
6	H + HCO = H$_2$ + CO	7.340×10^{13}	0.000	0
7	OH + HCO = H$_2$O + CO	5.000×10^{13}	0.000	0
8	HCO + H$_2$O = H + CO + H$_2$O	2.244×10^{18}	−1.000	17,000
9	H + CH$_2$O = HCO + H$_2$	2.300×10^{10}	1.050	3,275
10	O + CH$_2$O = OH + HCO	3.900×10^{13}	0.000	3,540
11	OH + CH$_2$O = HCO + H$_2$O	3.430×10^{9}	1.180	−447
12	O + CH$_3$ = H + CH$_2$O	8.430×10^{13}	0.000	0
13	CH$_3$ + O$_2$ = O + CH$_3$O	2.675×10^{13}	0.000	28,800
14	H + CH$_3$(+M) = CH$_4$(+M)	——	——	——
	k_∞	1.270×10^{16}	−0.630	383
	k_0	2.477×10^{33}	−4.760	2,440
	Troe/0.7830, 74.00, 2941.00, 6964.00			
15	H + CH$_4$ = CH$_3$ + H$_2$	6.600×10^{8}	1.620	10,840
16	O + CH$_4$ = OH + CH$_3$	1.020×10^{9}	1.500	8,600
17	OH + CH$_4$ = CH$_3$ + H$_2$O	1.000×10^{8}	1.600	3,120
18	H + CH$_2$O(+M) = CH$_3$O(+M)	——	——	——
	k_∞	5.400×10^{11}	0.454	2,600
	k_0	2.200×10^{30}	−4.800	5,560
	Troe/0.7580, 94.00, 1555.00, 4200.00			
19	2CH$_3$(+M) = C$_2$H$_6$(+M)	——	——	——
	k_∞	2.120×10^{16}	−0.970	620
	k_0	1.770×10^{50}	−9.670	6,220
	Troe/0.5325, 151.00, 1038.00, 4970.00			

Note: $k_f = AT^n \exp(-E_k/RT)$; units are in second, moles, centimeters, calories, and Kelvins.
Third body efficiencies:
(4) H$_2$ = 0.73, H$_2$O = 3.65, CH$_4$ = 2.00, C$_2$H$_6$ = 3.00
(14) H$_2$ = 2.00, H$_2$O = 6.00, CH$_4$ = 2.00, CO = 1.50, CO$_2$ = 2.00, C$_2$H$_6$ = 3.00
(18) H$_2$ = 2.00, H$_2$O = 6.00, CH$_4$ = 2.00, CO = 1.50, CO$_2$ = 2.00, C$_2$H$_6$ = 3.00
(19) H$_2$ = 2.00, H$_2$O = 6.00, CH$_4$ = 2.00, CO = 1.50, CO$_2$ = 2.00, C$_2$H$_6$ = 3.00

2.   Rods

Numerical simulations of the experiments on two-dimensional rods conducted by Srulijes et al.,[22] at the French–German ISL Institute, are presented by Yungster and Rabinowitz,[6] Soetrisno et al.,[3] and ourselves. In our calculations, the 14-species, 19-step reaction model with Troe formulas is used. The numerical results obtained using three different mesh sizes (76×51, 101×81, and 151×101) are nearly the same. This implies that the numerical simulations are not dependent on the mesh sizes in these steady combustion cases.

The two-dimensional rods were placed in a stoichiometric methane–air mixture at superdetonative velocity 2330 m/s in condition 3. The computed Chapman–Jouguet (C–J) detonation speed is $U_{CJ} \cong 1800$ m/s. Figure 5 shows the computational results for three cylindrical rods of the various diameters of 1, 3, and 7 mm. Yungster and Rabinowitz[6] and our computations predict the decoupled bow shock and reaction front profiles; however, the computations by Soetrisno et al.,[3] using the 9-species 12-step model show the fully coupled shock-deflagration wave. This demonstrates the ability of the reduced 19-step model to qualitatively predict the decoupled bow shock and reaction front profiles for the three rods. However, the temperature profiles behind the deflagration wave calculated using the 19-step model are different from the ones obtained using the Yungster and Rabinowitz model. This is because the 14-species and 19-step model predicted lower heat release and temperature distribution than did that of Yungster and Rabinowitz.

3.   Hemispheric Projectile

Figure 6 shows the density counters of the three numerical simulations various freestream pressures, 20, 10, and 6.4 kPa in conditions 4, 5, and 6, respectively. Note that the freestream pressure in the PLIF experimental condition 6 is eight times lower than the previous rod simulation (condition 3). The numerical simulations at $p_\infty = 20$ and 10 kPa show reaction fronts; however, the one at
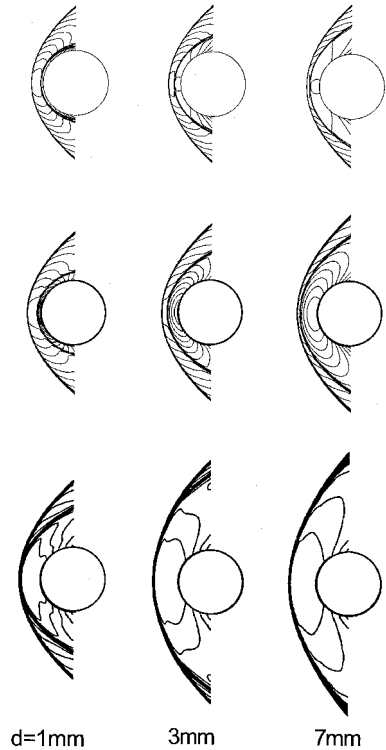

d=1mm   3mm   7mm

Fig. 5   Temperature contours around the two-dimensional rods by the present analyses (upper rank and mesh size 151×101), Yungster and Rabinowitz (middle rank and mesh size 91×91), and Soetrisno et al.[3] (lower rank and mesh size 72×65) in condition 3. The rod diameters are 1, 3, and 7 mm.
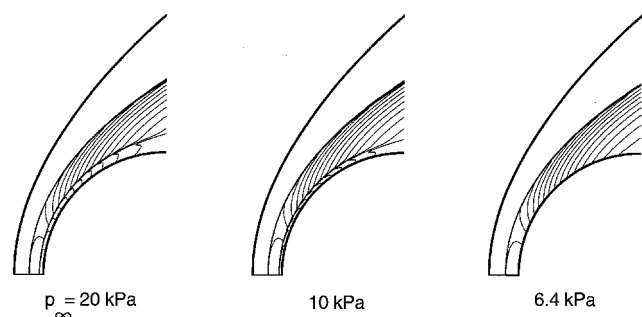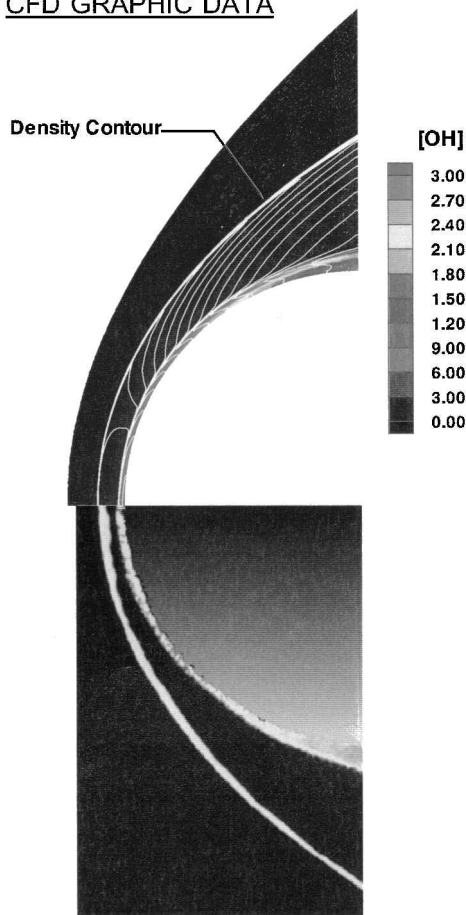
Fig. 6 Comparison of density contours around the hemispheric bodies in conditions 4, 5, and 6. The freestream pressures are various as 20, 10, and 6.4 kPa.

Fig. 7 Comparison of OH species density distributions and bow-shock profiles by CFD calculation, OH PLIF, and schlieren imaging results around the hemispheric body in condition 6.

6.4 kPa does not indicate the reaction front. This is because the Troe formulas may not activate recombination reaction steps 14, 18, and 19 at low pressure. This means that the pressure-dependent reaction coefficients in the reduced mechanism cause an incorrect ignition condition at the very low pressure. To avoid the incorrect ignition, we will omit the Troe formulas from the reduced mechanism under pressure 10 kPa.

Figure 7 shows the comparison of experimental results[12] with the numerical simulation using the reduced model of Table 3 without the pressure dependence of rate coefficients of the Troe formulas at condition 6 of the superdetonative mode. The computed C–J velocity of this case is 1958 m/s. Both OH species distributions and bow-shock profiles are in qualitative agreement.

These calculations required 6920 iterations and $\sim$10 h CPU time on a Hewlett Packard HP 9000/712. This means that this calculation does not need large computational power.

IV. Conclusions

Comparisons between CFD calculations and PLIF and schlieren measurements of air and shock-induced combustion around blunt projectiles are presented. Hydrogen–oxygen–nitrogen and methane–oxygen–nitrogen mixtures are considered for the combustible flows. In particular, a new reduced model consisting of 14 reaction species and 19 chemical steps is proposed to simulate the methane combustion for the expansion tube experiments. The numerical calculations and experimental imaging results for both mixtures are in qualitative agreement. It is concluded that the CFD code can be satisfactorily used for estimating the characteristics of bow-shock and reaction front profiles of flowfields around hypersonic projectiles.

References

[1]Wilson, G. J., and MacComack, R. W., "Modeling Supersonic Combustion Using a Fully Implicit Numerical Method," *AIAA Journal*, Vol. 30, No. 4, 1992, pp. 1008–1015.

[2]Wilson, G. J., and Sussman, M. A., "Computation of Unsteady Shock-Induced Combustion Using Logarithmic Species Conservation Equations," *AIAA Journal*, Vol. 31, No. 2, 1993, pp. 294–301.

[3]Soetrisno, M., Imlay, S. T., and Roberts, D. W., "Numerical Simulations of the Transdetonative Ram Accelerator Combusting Flow Field on a Parallel Computer," AIAA Paper 92-3249, July 1992.

[4]Li, C., Kailasanath, K., and Oran, E. S., "Detonation Structures on Ram-Accelerator Projectiles," AIAA Paper 94-0551, Jan. 1994.

[5]Yungster, S., Eberhardt, S., and Bruckner, A. P., "Numerical Simulation of Hypervelocity Projectiles in Detonable Gases," *AIAA Journal*, Vol. 29, No. 2, 1991, pp. 187–199.

[6]Yungster, S., and Rabinowitz, M. J., "Computation of Shock-Induced Combustion Using a Detailed Methane-Air Mechanism," *AIAA Journal*, Vol. 10, No. 5, 1994, pp. 609–617.

[7]Nusca, M. J., "Numerical Simulation of Fluid Dynamics with Finite-Rate and Equilibrium Combustion Kinetics for the 120-mm Ram Accelerator," AIAA Paper 93-2182, June 1993.

[8]Nusca, M. J., "Investigation of Ram Accelerator Flows for High Pressure Mixtures of Various Chemical Compositions," AIAA Paper 96-2946, July 1996.

[9]Ahuja, J. K., Kumar, A., Singh, D. J., and Tiwari, S. N., "Simulation of Shock-Induced Combustion Past Blunt Projectiles Using Shock-Fitting Technique," *Journal of Propulsion and Power*, Vol. 12, No. 3, 1996, pp. 518–526.

[10]Matsuo, A., Fujii, K., and Fujiwara, T., "Flow Features of Shock-Induced Combustion Around Projectile Traveling at Hypervelocities," *AIAA Journal*, Vol. 33, No. 6, 1995, pp. 1056–1063.

[11]Matsuo, A., and Fujii, K., "Detailed Mechanism of the Unsteady Combustion Around Hypersonic Projectiles," *AIAA Journal*, Vol. 34, No. 10, 1996, pp. 2082–2089.

[12]Kamel, M. R., Morris, C. I., Stouklov, I. G., and Hanson, R. K., "Imaging of Hypersonic Reactive Flow Around Cylinders and Wedges," Western State Section/The Combustion Inst. 1995 Fall Meeting at Stanford Univ., Paper 95F-196, Oct. 1995.

[13]Kamel, M. R., Morris, C. I., and Hanson, R. K., "Simulation PLIF and Schlieren Imaging of Hypersonic Reactive Flows Around Blunted Cylinders," AIAA Paper 97-0913, Jan. 1997.

[14]Houwing, A. F. P., Kamel, M. R., Morris, C. I., Wehe, S. D., Boyce, R. R., Thurber, M. C., and Hanson, R. K., "PLIF Imaging and Thermometry of NO/N2 Shock Layer Flows in an Expansion Tube," AIAA Paper 96-0537, Jan. 1996.

[15]Yee, H. C., "Upwind and Symmetric Shock Capturing Schemes," NASA TM 89464, 1987.

[16]Jachimowski, C. J., "An Analytical Study of the Hydrogen-Air Reaction Mechanism with Application to Scramjet Combustion," NASA TP-2791, Feb. 1988.

[17]Frenklach, M., Wang, H., Goldenberg, M., Smith, G. P., Golden, D. M., Bowman, C. T., Hanson, R. K., Gardiner, W. C., and Lissianski, V., "GRI-Mech—An Optimized Detailed Chemical Reaction Mechanism for Methane Combustion," Topical Rept., GRI-95/0058, Nov. 1995.

[18]Petersen, E. L., Davidson, D. F., Röhrig, M., Hanson, R. K., and Bowman, C. T., "A Shock Tube Study of High-Pressure Methane Oxidation," Western State Section/The Combustion Inst. 1995 Fall Meeting at Stanford Univ., Paper 95F-153, Oct. 1995.

[19]Lutz, A. E., Rupley, F. M., and Miller, J. A., "SENKIN: A Fortran Program for Predicting Homogeneous Gas Phase Chemical Kinetics with Sensitivity Analysis," Sandia National Lab., SAND87-8248, Livermore, CA, 1988.

[20]Kee, R. J., Rupley, F. M., and Miller, J. A., "Chemkin-II: A Fortran Chemical Kinetics Package for the Analysis of Gas-Phase Chemical Kinetics," Sandia National Lab., SAND89-8009, UC-4001, Livermore, CA, 1989.

[21]Gilbert, R. G., Luther, K., and Troe, J., "Ber. Bunsenges," *Physical Chemistry*, Vol. 87, 1983, p. 169.

[22]Srulijes, J., Smeets, G., and Seiler, F., "Expansion Tube Experiments for the Investigation of Ram-Accelerator-Related Combustion and Gasdynamic Problems," AIAA Paper 92-3246, July 1992.